

<sup>1</sup> Local host tree density increases forest insect disturbance severity,  
<sup>2</sup> but host size effect depends on climatic water deficit

<sup>3</sup> Michael J. Koontz<sup>1,2,\*</sup>, Andrew M. Latimer<sup>1,2</sup>, Leif A. Mortenson<sup>3</sup>, Christopher J. Fettig<sup>3</sup>, Malcolm P.  
<sup>4</sup> North<sup>1,2,4</sup>

<sup>5</sup> <sup>1</sup>Graduate Group in Ecology, University of California, Davis, CA, USA

<sup>6</sup> <sup>2</sup>Department of Plant Sciences, University of California, Davis, CA, USA

<sup>7</sup> <sup>3</sup>USDA Forest Service, Pacific Southwest Research Station, Placerville, CA, USA

<sup>8</sup> <sup>4</sup>USDA Forest Service, Pacific Southwest Research Station, Davis, CA, USA

<sup>9</sup> \*Correspondence: michael.koontz@colorado.edu

<sup>10</sup> Date report generated: April 06, 2019

<sup>11</sup> **Abstract**

<sup>12</sup> Bark beetles are a primary mortality agent of trees in western U.S. forests, and the recent Californian hot  
<sup>13</sup> drought of 2012 to 2015 created favorable conditions for bark beetle-induced tree mortality throughout the  
<sup>14</sup> yellow pine/mixed-conifer forest system in the Sierra Nevada mountain range. The western pine beetle,  
<sup>15</sup> *Dendroctonus brevicomis*, is the forest insect that is largely responsible for the especially common deaths of its  
<sup>16</sup> main host in California, the ponderosa pine tree (*Pinus ponderosa*). While previous work has demonstrated a  
<sup>17</sup> link between climate conditions related to tree water stress and forest density on the severity of the western  
<sup>18</sup> pine beetle disturbance, it remains challenging to disentangle the relative effects of these variables. Further,  
<sup>19</sup> forest density can affect western pine beetle behavior in a number of ways, which creates a need for more  
<sup>20</sup> information on complex forest structure (including local density, tree size, and the heterogeneity of these  
<sup>21</sup> variables across a forest stand) to uncover the most likely mechanism.

<sup>22</sup> We conducted aerial surveys over an established network of 32 permanent vegetation monitoring plots along  
<sup>23</sup> a 350km and 1000m elevation gradient in the Sierra Nevada mountain range of California using a small,  
<sup>24</sup> unhumanned aerial system (sUAS aka drone) equipped with a narrow-band multispectral camera. Using  
<sup>25</sup> Structure from Motion (SfM) processing on over 450,000 images, we reconstructed the complex vegetation  
<sup>26</sup> structure of over 9 square kilometers of forest that experienced ponderosa pine mortality as a result of  
<sup>27</sup> western pine beetle activity. Using this dataset, we built a model to predict the probability of ponderosa  
<sup>28</sup> pine mortality as a function of forest structure variables (including ponderosa pine density and mean size, as  
<sup>29</sup> well as all tree density and mean size), an environmental gradient of climatic water deficit, and a Gaussian

30 process to capture spatial covariance in the response.

31 Data from small, unhummaned aerial systems (sUAS) can provide important context surrounding ground  
32 plots, which enables inference and generates new insights into ecological processes. sUAS are best-suited to  
33 enhancing ground data, which implies that we need not abandon lessons learned from sound experimental  
34 design (i.e., a network of plots along a gradient is still a powerful way to use sUAS data).

35 Host availability for aggressive bark beetles appears to have played the dominant role in increasing the  
36 probability of ponderosa pine mortality in the most hard-hit forest stands during the cumulative mortality  
37 event of 2012 to 2018. Host size played a role in its interaction with environmental condition– climatic  
38 water deficit– such that numerous and smaller host trees increased the probability of ponderosa mortality at  
39 cool/wet sites, while numerous and larger host trees increased the probability of ponderosa mortality at  
40 hot/dry sites.

41 Our results corroborate the role of host tree density and regional climate conditions on the severity of forest  
42 insect disturbance, but also highlight the importance of complex forest structure (i.e., both host density and  
43 average host size) in its interaction with regional climate. Thus, the future forest structure may be affected  
44 differently by a large-scale forest insect disturbance for the same host tree/forest insect pairing, and during  
45 the same extreme drought, but across a gradient of regional climate conditions.

## 46 **Introduction**

47 Framing: environmental drivers of insect severity, forest structure drivers of insect severity,

48 Aggressive bark beetles dealt the final blow to many of the nearly 150 million trees killed in the California  
49 drought of 2012 to 2015 and its aftermath (USDAFS 2019). A harbinger of climate change effects to come,  
50 high temperatures exacerbating the extreme drought led to tree mortality events of unprecedented size in the  
51 driest, densest forests across the state (Millar and Stephenson 2015, Young et al. 2017). A century of fire  
52 suppression policy has enabled forests to grow into dense stands, which increases water stress on trees and  
53 makes them more vulnerable to bark beetle attack (Fettig 2012, North et al. 2015).

54 Forests in California’s Sierra Nevada region are characterized by regular bark beetle disturbances that interact  
55 with forest structure. Bark beetles shape forest structure as they sporadically kill weakened trees under  
56 normal conditions, or wide swaths of even healthy trees under outbreak conditions (Raffa et al. 2015). Forest  
57 structure also strongly influences bark beetle activity. Low-density forests are less prone to bark beetle  
58 attacks (Fettig 2012), but resolving the mechanism underlying this observation requires a more nuanced view  
59 of forest structure. For instance, a low-density forest may resist attack because longer dispersal distances are

60 required for successful colonization of new hosts, because widely-spaced trees experience less competition  
61 for water resources and thus average tree vigor is greater (Hayes et al. 2009), or because its wider canopy  
62 openings disrupt pheromone signaling between beetles (Fettig 2012).

63 Tree density is often a coarse gauge of the size and spatial distribution of trees— the forest structure— with  
64 which bark beetles interact (Raffa et al. 2008). Climate change mitigation strategies emphasize reducing tree  
65 densities (North et al. 2015, Young et al. 2017), but understanding the optimal scale and pattern of tree  
66 distribution that can mitigate bark beetle outbreaks will be vital for predicting how California forests may  
67 respond to these interventions. Recent research has shown a strong link between complex forest structure  
68 and forest resilience, but measuring this complexity generally requires expensive equipment or labor-intensive  
69 field surveys (Larson and Churchill 2012, Kane et al. 2014). These barriers restrict survey frequency and  
70 extent, which limits insights into phenomena like bark beetle outbreaks that rapidly emerge over weeks to  
71 months but have long-lasting effects on forest conditions. Further, the vast spatial extent and environmental  
72 gradient of mortality (Young et al. 2017, USDAFS 2019) challenges our ability to simultaneously consider  
73 how environmental conditions may interact with local forest structure to produce patterns of insect activity.  
74 Small, unhumanned aerial systems (sUAS) enable fast and relatively cheap remote imaging over dozens of  
75 hectares of forest, which can be used to determine both forest structure and tree condition at the individual  
76 tree scale (Morris et al. 2017, Shiklomanov et al. 2019).

77 We used ultra-high resolution remote sensing data from a small, unhumanned aerial system over a network of  
78 32 sites in the Sierra Nevada spanning 1000m of elevation and 350km of latitude and covering a total of 9  
79 square kilometers of forest to ask how fine-scale forest structure affected the probability of tree mortality  
80 during the cumulative mortality event of 2012 to 2018. We asked:

- 81 1. How does local host tree density and size affect the severity of western pine beetle disturbance?
- 82 2. How does total tree density and size affect the severity of western pine beetle disturbance?
- 83 3. How does environmentally-driven tree moisture stress affect the severity of western pine beetle distur-  
84 bance?
- 85 4. Do the effects of forest structure and environmental condition on western pine beetle disturbance  
86 interact?

87 Which trees die during drought? Gradient of stress to host selection. Stephenson et al. (2019) argue that  
88 there are differences across species during an extreme drought on whether environment or forest structure  
89 drives mortality. But even within the same species, there could be *interaction* between the background

90 environmental condition and the forest struture in driving mortality that gives rise to stress-dominated  
91 mortality in some locations and host-selection dominated mortality in other locations *for the same species*.

## 92 Methods

### 93 Study system

94 The study sites comprise mostly ponderosa pine trees, *Pinus ponderosa*, whose primary bark beetle predator  
95 in California is the western pine beetle (WPB), *Dendroctonus brevicomis*. The WPB is an aggressive bark  
96 beetle, meaning it must attack and kill live trees in order to successfully reproduce (Raffa et al. 2008).  
97 Pioneer WPBs disperse to a new host tree, determine the host's susceptibility to attack, and use pheromone  
98 signals to attract other WPBs. The attracted WPBs mass attack the tree by boring into its inner bark,  
99 laying eggs, and dying, leaving their offspring to develop inside the doomed tree before themselves dispersing  
100 (Raffa et al. 2008). Small WPB populations prefer weakened trees but large populations can overwhelm  
101 the defense mechanisms of even healthy trees. Successful attacks on large, healthy trees are boons to bark  
102 beetle fecundity and trigger outbreaks in which populations explode and massive tree mortality occurs. In  
103 California, the WPB can have 3 generations in a single year giving it a greater potential to spread rapidly  
104 through forests than its more infamous congener, the mountain pine beetle, *Dendroctonus ponderosa* (MPB).

105 We built our study on 180 vegetation/forest insect monitoring plots at 36 sites established between 2016 and  
106 2017 (Fettig et al. 2019). These established plots were located in beetle-attacked, mixed-conifer forests across  
107 the Eldorado, Stanislaus, Sierra and Sequoia National Forests and were stratified by elevation (914-1219  
108 meters [3000-4000 feet], 1219-1524 meters [4000-5000 feet], 1524-1828 meters [5000-6000 feet] above sea level).  
109 In the Sequoia National Forest, the National Forest that is furthest south, plots were stratified with the lowest  
110 elevation band between 1219 and 1524 (4000-5000 feet) and extended to an upper elevation band of 1828-2133  
111 (6000-7000 feet) to capture a more similar forest community composition as at the more northern National  
112 Forests. The sites have variable forest structure and disturbance history and plot locations were selected  
113 specifically in areas with >40% ponderosa pine basal area and >10% ponderosa pine mortality. The 0.04ha  
114 circular plots are clustered along transects in groups of 5, with between 80 and 200m between each plot. All  
115 trees within the plot were assessed as dead or alive. The stem location of all trees was mapped relative to the  
116 center of each plot using azimuth/distance measurements. Tree identity to species and diameter at breast  
117 height (dbh) were recorded if dbh was greater than 6.35cm. During the spring and early summer of 2018, all  
118 field plots were revisited to assess whether dead trees had fallen (Fettig et al. 2019).

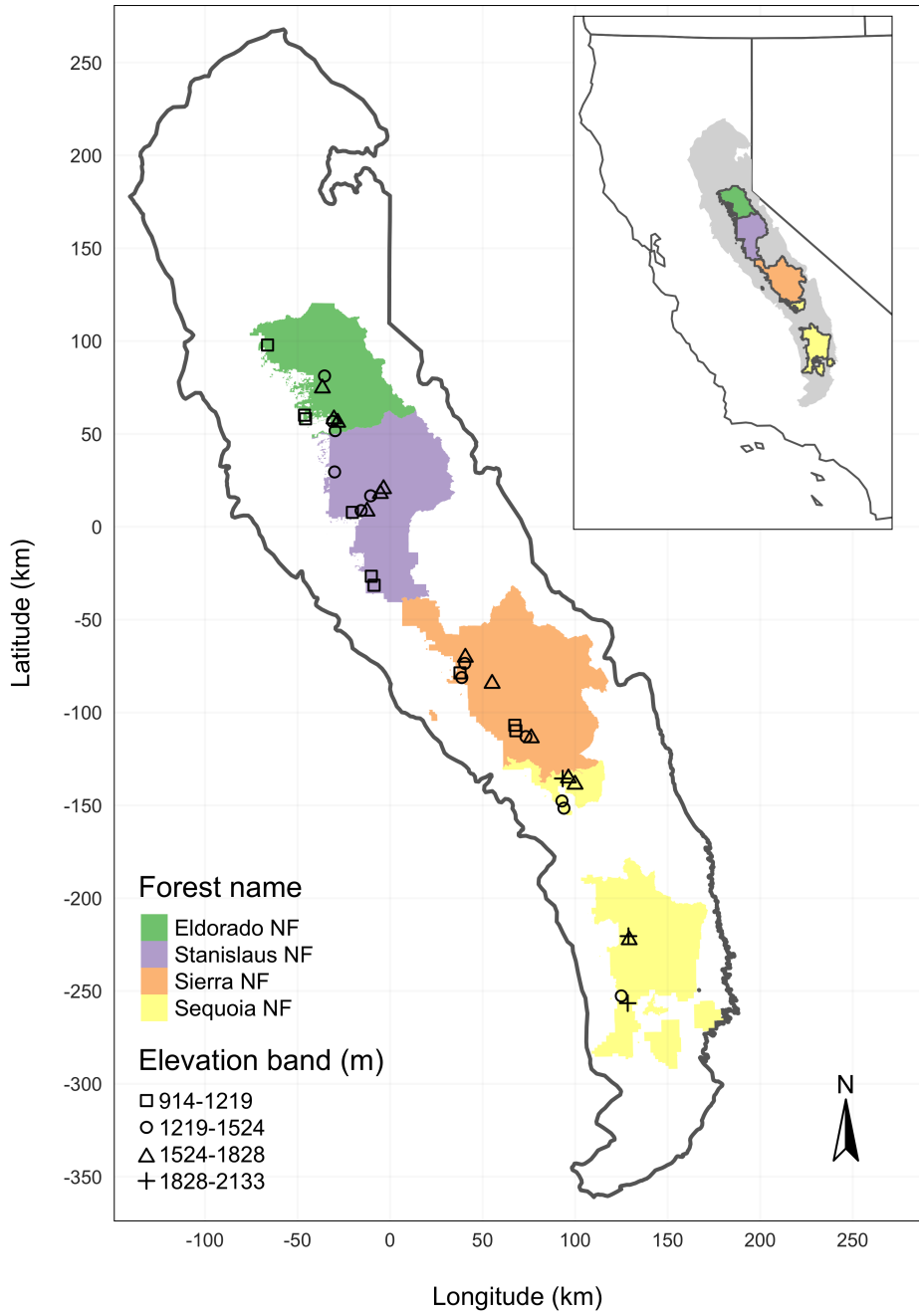


Figure 1: The network of field plots spanned a 350 km latitudinal gradient from the Eldorado National Forest in the north to the Sequoia National Forest in the south. Plots were stratified by three elevation bands in each forest, with the plots in the Sequoia National Forest (the southern-most National Forest) occupying elevation bands 305m above the three bands in the other National Forests in order to capture a similar community composition.

119 **Instrumentation**

120 Imagery was captured using a DJI Zenmuse X3 RGB camera (DJI 2015a) and a Micasense RedEdge3 5-band  
121 multispectral camera (Micasense 2015). We mounted both of these instruments simultaneously on a DJI  
122 Matrice 100 aircraft (DJI 2015b) using the DJI 3-axis stabilized gimbal for the Zenmuse X3 camera and a  
123 Micasense angled fixed mount for the RedEdge3 camera. The gimbal and the angled fixed mount ensured  
124 both instruments were nadir-facing during image capture. Just prior or after image capture at each site, we  
125 calibrated the RedEdge3 camera by taking an image of a calibration panel on the ground in full sun with  
126 known reflectance values for each of the 5 narrow bands.

Table 1: Reflectance sensitivity of the Micasense Rededge3 camera. The calibration panel value represents the reflectance of the calibration panel for the given wavelength.

Band number	Band name	Center wavelength	Band width	Wavelength range	Panel reflectance
1	blue (b)	475	20	465-485	0.64
2	green (g)	560	20	550-570	0.64
3	red (r)	668	10	663-673	0.64
4	near infrared (nir)	840	40	820-860	0.60
5	red edge (re)	717	10	712-722	0.63

127 **Flight protocol**

128 Image capture was conducted as close to solar noon as possible to minimize shadow effects (always within 4  
129 hours; usually within 2 hours). Prior to the aerial survey, two strips of bright orange drop cloth (~100cm x  
130 15cm) were positioned as an “X” over the permanent monuments marking the center of the 5 field plots from  
131 Fettig et al. (2019).

132 For each of the 36 sites (containing 5 plots each), we captured imagery over the surrounding ~40 hectares  
133 of forested area using north-south aerial transects. For XXXXX sites, we surveyed less surrounding area  
134 in order to maintain visual and radio communication with the aircraft during flight (Table XXXXXX; as a  
135 supplement, I think; Columns: Site, forest, elevation, rep, CWD, surveyed area, survey date).

136 We preprogrammed transect paths using Map Pilot for DJI on iOS (hereafter Map Pilot) (Easy 2018). All  
137 transects tracked the terrain and their altitude remained approximately constant at 120 meters above ground  
138 level in order to maintain consistent ground sampling distance in the imagery. Ground level was based on a

<sup>139</sup> 1-arc-second digital elevation model (Farr et al. 2007) and we implemented terrain following using Map Pilot.  
<sup>140</sup> For this analysis, we dropped 4 sites whose imagery was of insufficient quality to process.

<sup>141</sup> Structure from motion (SfM) processing requires highly overlapping images, especially in densely vegetated  
<sup>142</sup> areas. We planned transects with 90% forward overlap and 90% side overlap at 100 meters below the lens.  
<sup>143</sup> Thus, with flights being at 120 meters above ground level, we achieved slightly higher than 90/90 overlap for  
<sup>144</sup> objects 20 meters tall or shorter (91.6/91.6 overlap at the ground). Overlap values were based on focal length  
<sup>145</sup> (3.6mm), sensor width (6.2mm), and image dimension (4000x3000 pixels) parameters of the Zenmuse X3  
<sup>146</sup> camera. Images were captured at a constant rate of 1 image every 2 seconds for both cameras. A forward  
<sup>147</sup> overlap of 90% at 100 meters translates to a flight speed of approximately 6.45 m/s and a side overlap of 90%  
<sup>148</sup> at 100 meters translates to transects approximately 17.2 meters apart. The Rededge camera has a different  
<sup>149</sup> focal length (5.4mm), sensor width (4.8mm), and image dimension (1280x960 pixels), which translates to  
<sup>150</sup> image overlap of 80.7/80.7 at 100m below the lens and 83.9/83.9 at ground level. Approximately 1900 photos  
<sup>151</sup> were captured over each 40 hectare survey area for each camera.

## <sup>152</sup> **Structure from motion/Photogrammetric processing**

<sup>153</sup> We used structure from motion (SfM), aka photogrammetry, to generate orthorectified reflectance maps,  
<sup>154</sup> digital surface models, and dense point clouds for each field site. We used Pix4Dmapper Cloud to process  
<sup>155</sup> imagery using parameters ideal for images of a densely vegetated area taken by a multispectral camera.  
<sup>156</sup> For three sites, we processed the RGB and the multispectral imagery in the same project to enhance the  
<sup>157</sup> resolution of the dense point cloud. All SfM projects resulted in a single processing “block,” indicating that  
<sup>158</sup> all images in the project were optimized and processed together.

## <sup>159</sup> **Creating canopy height models**

<sup>160</sup> We classified each survey area’s dense point cloud into “ground” and “non-ground” points using a cloth  
<sup>161</sup> simulation filter algorithm (Zhang et al. 2016) implemented in the **lidR** (Roussel et al. 2019) package. We  
<sup>162</sup> rasterized the ground points using the **raster** package (Hijmans et al. 2019) to create a digital terrain model  
<sup>163</sup> representing the ground underneath the vegetation at 1 meter resolution. We created a canopy height model  
<sup>164</sup> by subtracting the digital terrain model from the digital surface model created in Pix4Dmapper.

## <sup>165</sup> **Tree detection**

<sup>166</sup> We tested a total of 7 automatic tree detection algorithms and a total of 177 parameter sets on the canopy  
<sup>167</sup> height model or the dense point cloud to locate trees within each site (Table XXXXX; algorithm, number of

parameter sets, reference). We used 3 parameter sets of a variable window filter implemented in `ForestTools` (Plowright 2018) including the default variable window filter function in `ForestTools` as well as the “pines” and “combined” functions from Popescu and Wynne (2004). We used 6 parameter sets of a local maximum filter implemented in `lidR`. We used 131 parameter sets of the algorithm from Li et al. (2012), which operates on the original point cloud. These parameter sets included those from Shin et al. (2018) and Jakubowski et al. (2013). We used 3 parameter sets of the `watershed` algorithm implemented in `lidR`, which is a wrapper for a function in the `EBImage` package (Pau et al. 2010). We used 3 parameter sets of `ptrees` (Vega et al. 2014) implemented in `lidR` (Roussel et al. 2019) and `lidRplugins` (Roussel 2019) and which operates on the raw point cloud, without first normalizing it to height above ground level (i.e.. subtracting the ground elevation from the dense point cloud). We used the default parameter set of the `multichm` (Eysn et al. 2015) algorithm implmented in `lidR` (Roussel et al. 2019) and `lidRplugins` (Roussel 2019). We used 30 parameter sets of the experimental algorithm `lmfx` (Roussel 2019).

## Map ground data

Each orthorectified reflectance map was inspected to locate the 5 orange “X”s marking the center of the field plots. We were able to locate 110 out of 180 field plots and were then able to use these plots for validation of automated tree detection algorithms. We used the `sf` package (Pebesma et al. 2019) to convert distance-from-center and azimuth measurements of each tree in the ground plots to an x-y position on the SfM-derived reflectance map using the x-y position of the orange X visible in the reflectance map as the center.

## Correspondence of automatic tree detection with ground data

We calculated 7 forest structure metrics for each field plot using the ground data collected by Fettig et al. (2019): total number of trees, number of trees greater than 15 meters, number of trees less than 15 meters, mean height of trees, 25<sup>th</sup> percentile tree height, 75<sup>th</sup> percentile tree height, mean distance to nearest tree neighbor, mean distance to 2<sup>nd</sup> nearest neighbor.

For each tree detection algorithm and parameter set described above, we calculated the same set of 7 structure metrics within the footprint of the validation field plots. We calculated the Pearson’s correlation and root mean square error (RMSE) between the ground data and the aerial data for each of the 7 structure metrics for each of the 177 automatic tree detection algorithms/parameter sets.

For each algorithm and parameter set, we calculated its performance relative to other algorithms as whether its Pearson’s correlation was within 5% of the highest Pearson’s correlation as well as whether its RMSE was

198 within 5% of the lowest RMSE. For each algorithm/parameter set, we summed the number of forest structure  
199 metrics for which it reached these 5% thresholds. For automatically detecting trees across the whole study,  
200 we selected the algorithm/parameter set that performed well across the most number of forest metrics.

201 **Segmentation of crowns**

202 We delineated individual tree crowns with a marker controlled watershed segmentation algorithm (Meyer and  
203 Beucher 1990) using the detected treetops as markers implemented in the `ForestTools` package (Plowright  
204 2018). If the automatic segmentation algorithm failed to generate a crown segment for a detected tree (e.g.,  
205 often snags with a very small crown footprint), a circular crown was generated with a radius of 0.5 meters. If  
206 the segmentation generated multiple polygons for a single detected tree, only the polygon containing the  
207 detected tree was retained. Image overlap decreases near the edges of the overall flight path, which reduces  
208 the quality of the SfM processing in those areas. Thus, we excluded segmented crowns within 35 meters of  
209 the edge of the survey area.

210 We used the `velox` package (Hunziker 2017) to extract all the pixel values from the orthorectified reflectance  
211 map for each of the 5 narrow bands within each segmented crown polygon. Per pixel, we additionally  
212 calculated the normalized difference vegetation index (NDVI; Rouse et al. (1973)), the normalized difference  
213 red edge (NDRE; Gitelson and Merzlyak (1994)), the red-green index (RGI; Coops et al. (2006)), the red  
214 edge chlorophyll index (CI[red edge]; Clevers and Gitelson (2013)), and the green chlorophyll index (CI[green];  
215 Clevers and Gitelson (2013)). For each crown polygon, we calculated the mean value for each raw and derived  
216 reflectance band (5 raw; 5 derived).

217 **Classification of trees**

218 We overlaid the segmented crowns on the reflectance maps from 20 sites spanning the latitudinal and  
219 elevational gradient in the study. Using QGIS, we hand classified XXXX trees as live/dead and as one  
220 of 5 dominant species in the study area (*Pinus ponderosa*, *Pinus lambertiana*, *Abies concolor*, *Calocedrus*  
221 *decurrens*, or *Quercus kelloggii*) using the mapped ground data as a guide.

222 We used all 10 mean values of the reflectance bands for each tree crown polygon to predict whether the hand  
223 classified trees were alive or dead using a boosted logistic regression model implemented in the `caret` package  
224 (Kuhn 2008). For just the living trees, we similarly used all 10 reflectance values to predict the tree species  
225 using regularized discriminant analysis implemented in the `caret` package, which proved to have the highest  
226 accuracy for a training dataset (accuracy = XXXXX, kappa = XXXXX).

227 Finally, we used these models to classify all tree crowns in the data set as alive or dead as well as the species

228 of living trees.

229 **Allometric scaling of height to basal area**

230 We converted the height of each tree determined using the canopy height model to its basal area. Using  
231 the tree height and diameter at breast height (DBH; breast height = 1.37m) ground data from Fettig et al.  
232 (2019), we fit a simple linear regression to predict DBH from height for each of the 5 dominant species. Using  
233 the model-classified tree species of each segmented tree, we used the corresponding linear relationship for  
234 that species to estimate the DBH given the tree's height. We then calculated each tree's basal area, assuming  
235 no tapering from breast height.

236 **Note on assumptions about dead trees**

237 For the purposes of this study, we assumed that all dead trees were ponderosa pine and were thus host trees.  
238 This is a reasonably good assumption, given that Fettig et al. (2019) found that 73.4% of the dead trees in  
239 the coincident ground plots were ponderosa pine.

240 **Rasterizing individual tree data**

241 Because the tree detection algorithms were validated against ground data at the plot level, we rasterized the  
242 classified trees at a spatial resolution similar to that of the ground plots (rasterized to 20m x 20m equalling  
243 400 m<sup>2</sup>; circular ground plots with 11.35m radius equalling 404 m<sup>2</sup>). In each raster cell, we tallied: number  
244 of alive trees, number of dead trees, number of ponderosa pine trees, number of non-ponderosa pine trees,  
245 basal area of ponderosa pine trees, basal area of non-ponderosa pine trees.

246 **Environmental data**

247 We used climatic water deficit (CWD) (Stephenson 1998) from the 1980-2010 mean value of the basin  
248 characterization model (Flint et al. 2013) as an integrated measure of temperature and moisture conditions  
249 for each cell. Higher values of CWD correspond to hotter, drier conditions and lower values correspond  
250 to cooler, wetter conditions CWD has been shown to correlate well with broad patterns of tree mortality  
251 in the Sierra Nevada (Young et al. 2017). We resampled the climatic water deficit product using bilinear  
252 interpolation implemented in the `raster` package to match the 20m x 20m spatial scale of the other variables.  
253 We converted the CWD value for each cell into a z-score representing that cell's deviation from the mean  
254 CWD across the climatic range of Sierra Nevada ponderosa pine as determined from XXXXX herbarium  
255 records described in Baldwin et al. (2017). Thus, a CWD z-score of one would indicate that the CWD at

256 that cell is one standard deviation hotter/drier than the mean CWD across all geolocated herbarium records  
 257 for ponderosa pine in the Sierra Nevada.

258 **Statistical model**

259 We used a generalized linear model with a zero-inflated binomial response and a logit link to predict the  
 260 probability of ponderosa pine mortality within each raster cell as a function of the crossed effects of ponderosa  
 261 pine quadratic mean diameter and density added to the crossed effect of overall quadratic mean diameter and  
 262 density as well as the interaction of each summand with climatic water deficit at each site.

263 To measure and account for spatial autocorrelation of the bark beetle behavioral processes underlying  
 264 ponderosa mortality, we first subsampled the data at each site to a random selection of 200, 20m x 20m  
 265 cells representing approximately 27.5% of the surveyed area. With these subsampled data, we included a  
 266 separate exact Gaussian process term per site of the interaction between the x- and y-position of each cell  
 267 using the `gp()` function in the `brms` package (Bürkner 2017). The Gaussian process accounts for spatial  
 268 autocorrelation in the model by jointly estimating the spatial covariance of the response variable with the  
 269 effects of the other covariates.

$$y_{i,j} \sim \begin{cases} 0, & p \\ Binom(n_i, \pi_i), & 1 - p \end{cases}$$

$$\begin{aligned} logit(\pi_i) = & \beta_0 + \\ & \beta_1 X_{cwd,j} + \\ & \beta_1 X_{cwd,j} (\beta_2 X_{\text{pipoQMD},i} + \beta_3 X_{\text{pipoDensity},i} + \beta_4 X_{\text{pipoQMD},i} X_{\text{pipoDensity},i}) + \\ & \beta_1 X_{cwd,j} (\beta_5 X_{\text{overallQMD},i} + \beta_6 X_{\text{overallDensity},i} + \beta_7 X_{\text{overallQMD},i} X_{\text{overallDensity},i}) + \\ & \mathcal{GP}_j(x_i, y_i) \end{aligned}$$

270 Where  $y_i$  is the number of dead trees in cell  $i$ ,  $n_i$  is the sum of the dead trees and live ponderosa pine trees  
 271 in cell  $i$ ,  $\pi_i$  is the probability of ponderosa pine tree mortality in cell  $i$ ,  $p$  is the probability of there being  
 272 zero dead trees in a cell arising as a result of an unmodeled process,  $X_{cwd,j}$  is the z-score of climatic water  
 273 deficit for site  $j$ ,  $X_{\text{pipoQMD},i}$  is the scaled quadratic mean diameter of ponderosa pine in cell  $i$ ,  $X_{\text{pipoDensity},i}$   
 274 is the scaled density of ponderosa pine trees in cell  $i$ ,  $X_{\text{overallQMD},i}$  is the scaled quadratic mean diameter  
 275 of all trees in cell  $i$ ,  $X_{\text{overallDensity},i}$  is the scaled density of all trees in cell  $i$ ,  $x_i$  and  $y_i$  are the x- and y-  
 276 coordinates of the centroid of the cell in an EPSG3310 coordinate reference system, and  $\mathcal{GP}_j$  represents the

277 exact Gaussian process describing the spatial covariance between cells at site  $j$ .

278 We used 4 chains with 2000 iterations each (1000 warmup, 1000 samples), and confirmed chain convergence  
279 by ensuring all Rhat values were less than 1.1 (Brooks and Gelman 1998). We used posterior predictive  
280 checks to visually confirm model performance by overlaying the density curves of the predicted number of  
281 dead trees per cell over the observed number (Gabry et al. 2019). For the posterior predictive checks, we  
282 used 50 random samples from the model fit to generate 50 density curves and ensured curves were centered  
283 on the observed distribution, paying special attention to model performance at capturing counts of zero.

284 **Software and data availability**

285 All data are available via the Open Science Framework. Statistical analyses were performed using the **brms**  
286 packages. With the exception of the SfM software (Pix4Dmapper Cloud) and the GIS software QGIS, all  
287 data carpentry and analyses were performed using R (R Core Team 2018).

288 **Results**

Table 2: Site characteristics for each of the 32 sites. The site name consists of the forest name, elevation band, and rep separated by an underscore. The Eldorado National Forest is ‘elido’, the Stanislaus National Forest is ‘stan’, the Sierra National Forest is ‘sier’, and the Sequoia National Forest is ‘sequ’. The elevation band represents the lower bounds of the 305 meter (1000 foot) elevation bands in feet. Thus ‘3k’ implies that site was located between 3,000 and 4,000 feet (914-1219 meters). Aerially detected mortality and density of the whole site is presented along with the mortality and density calculated from the ground data (aerial / ground). The density is measured in trees per hectare (tpha).

Site	CWD (mm)	CWD (z-score)	Survey area (ha)	Mortality (aerial/ground)	Density (tpha; aerial/ground)
elido_3k_1	678.45	0.32	31.02	0.11/0.61	630.01/410.19
elido_3k_2	706.48	0.50	30.61	0.12/0.36	444.26/647.42
elido_3k_3	654.51	0.16	30.95	0.22/0.36	492.63/410.19
elido_4k_1	570.43	-0.38	28.04	0.09/0.39	632.82/588.11
elido_4k_2	642.20	0.08	28.41	0.15/0.78	338.20/271.82

Site	CWD (mm)	CWD (z-score)	Survey area (ha)	Mortality (aerial/ground)	Density (tpha; aerial/ground)
eldo_5k_1	663.09	0.22	28.44	0.11/0.44	661.80/543.63
eldo_5k_2	627.38	-0.01	30.02	0.12/0.36	584.89/968.65
eldo_5k_3	598.66	-0.20	29.73	0.07/0.32	488.66/622.71
stan_3k_1	638.49	0.06	31.04	0.10/0.52	739.45/1037.84
stan_3k_2	739.23	0.71	18.78	0.40/0.78	433.53/405.25
stan_3k_3	761.64	0.86	30.10	0.22/0.41	558.43/326.18
stan_4k_1	540.16	-0.58	29.62	0.29/0.63	507.61/711.66
stan_4k_2	528.07	-0.66	30.54	0.18/0.56	481.85/256.99
stan_5k_1	523.51	-0.69	30.94	0.19/0.54	388.89/336.06
stan_5k_2	523.95	-0.68	29.94	0.21/0.44	399.33/622.71
sier_3k_1	763.54	0.87	30.42	0.19/0.48	651.46/850.04
sier_3k_2	767.64	0.90	30.05	0.20/0.77	438.84/153.21
sier_3k_3	772.98	0.93	29.77	0.32/0.77	511.26/459.62
sier_4k_1	841.25	1.38	30.43	0.54/0.51	576.15/538.69
sier_4k_2	764.38	0.88	29.30	0.33/0.57	499.43/854.98
sier_4k_3	688.34	0.38	26.39	0.48/0.59	454.23/499.15
sier_5k_1	721.59	0.60	14.59	0.41/0.43	631.30/716.60
sier_5k_2	709.96	0.52	27.53	0.53/0.74	477.29/454.67
sier_5k_3	778.53	0.97	28.93	0.33/0.43	569.44/484.33
sequ_4k_1	766.61	0.89	29.59	0.50/0.56	365.81/607.88
sequ_4k_3	815.60	1.21	29.69	0.35/0.71	433.35/306.41
sequ_5k_1	718.24	0.58	27.12	0.35/0.52	364.01/444.79
sequ_5k_2	587.26	-0.27	29.10	0.45/0.43	478.31/499.15
sequ_5k_3	611.33	-0.12	31.34	0.42/0.48	348.68/494.21
sequ_6k_1	730.52	0.66	27.78	0.30/0.70	433.43/360.77
sequ_6k_2	689.51	0.39	11.83	0.26/0.43	699.04/934.06
sequ_6k_3	602.65	-0.17	26.51	0.36/0.32	535.54/691.89

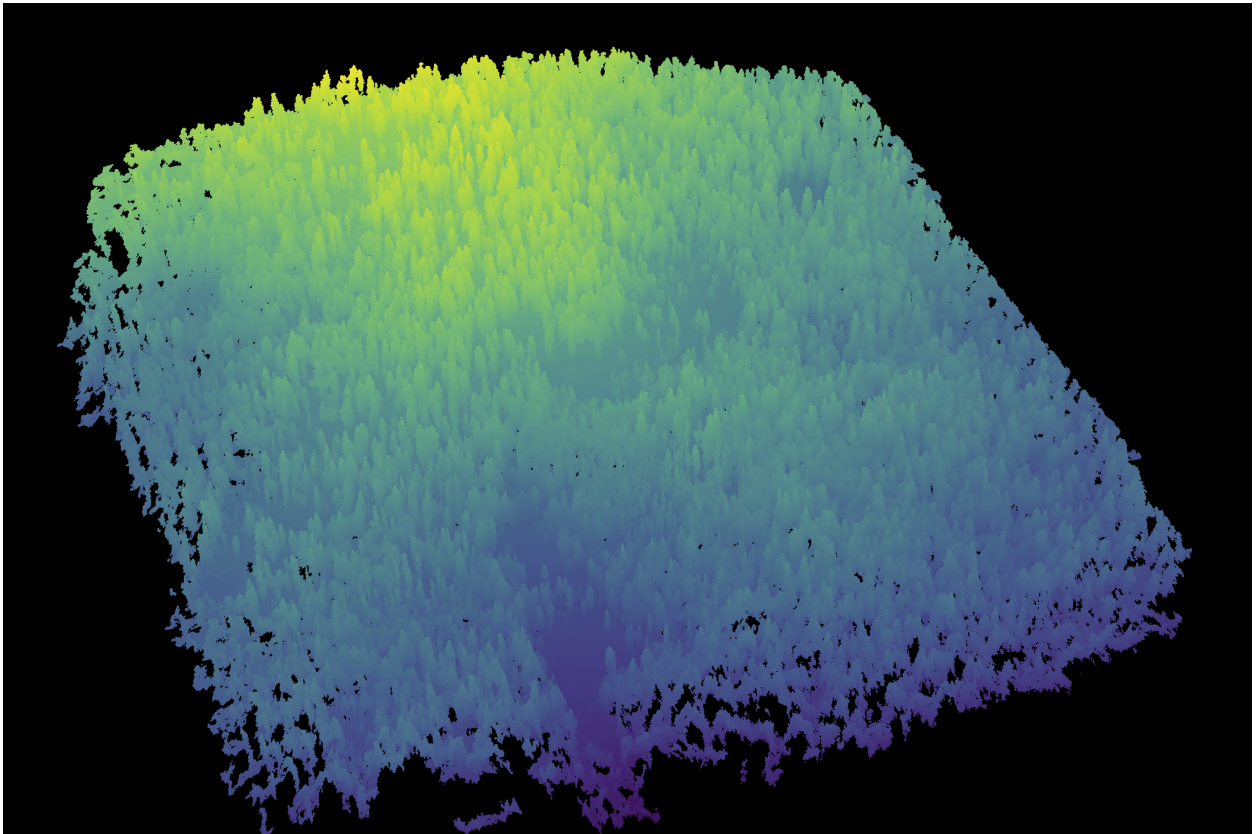


Figure 2: A dense point cloud representing ~40 hectares of forest is generated using Structure from Motion (SfM) processing of ~1900 images. The dense point cloud z- position represents the ground elevation plus the vegetation height.

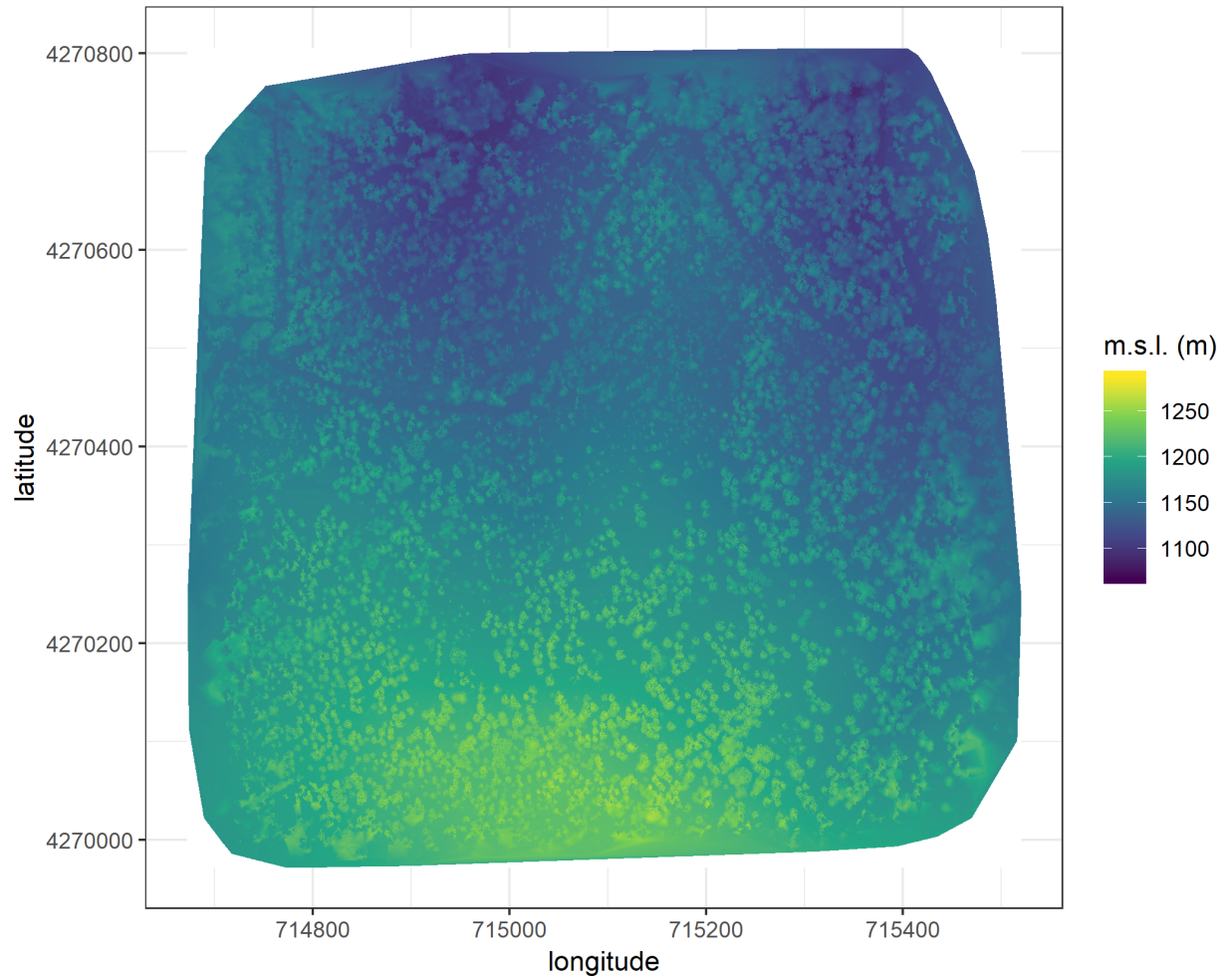


Figure 3: The digital surface model (DSM) is a 2-dimensional representation of the dense point cloud generated using structure from motion (SfM) processing. The DSM represents the ground elevation plus the vegetation height.

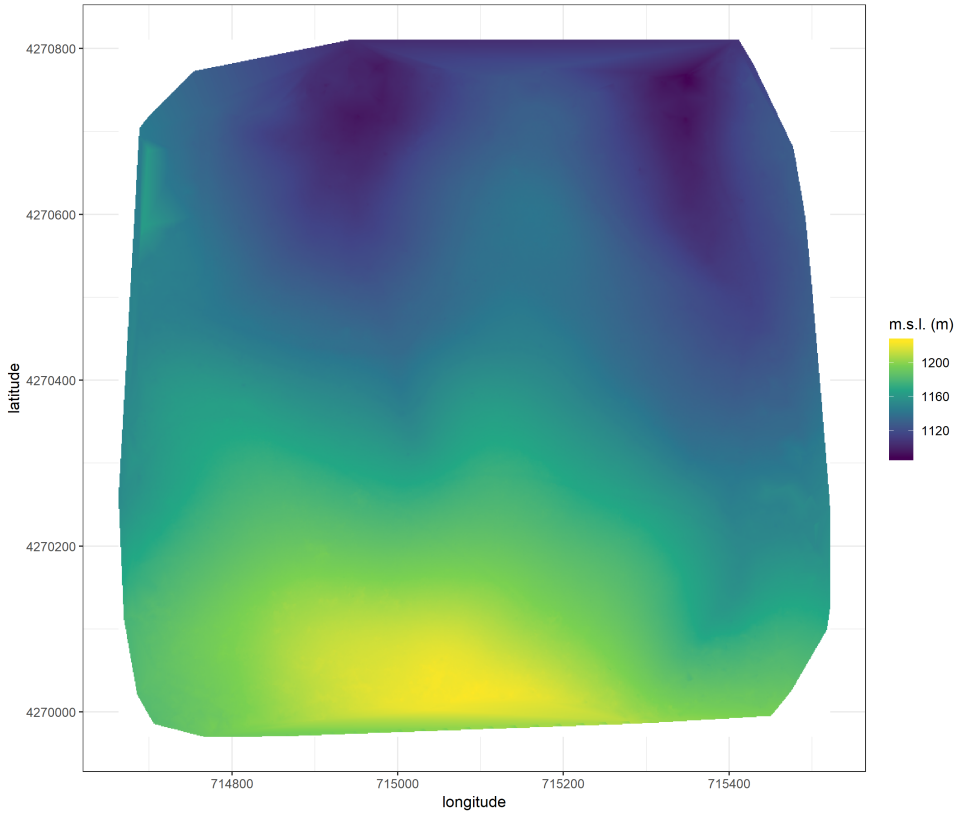


Figure 4: The digital terrain model (DTM) is generated by processing the dense point cloud using the cloth simulation filter algorithm (Zhang et al. 2016), which classifies points as “ground” or “not-ground” and then interpolates the “ground” elevation using Delaunay triangulation for the rest of the dense point cloud footprint. The DTM represents the ground elevation without any vegetation.

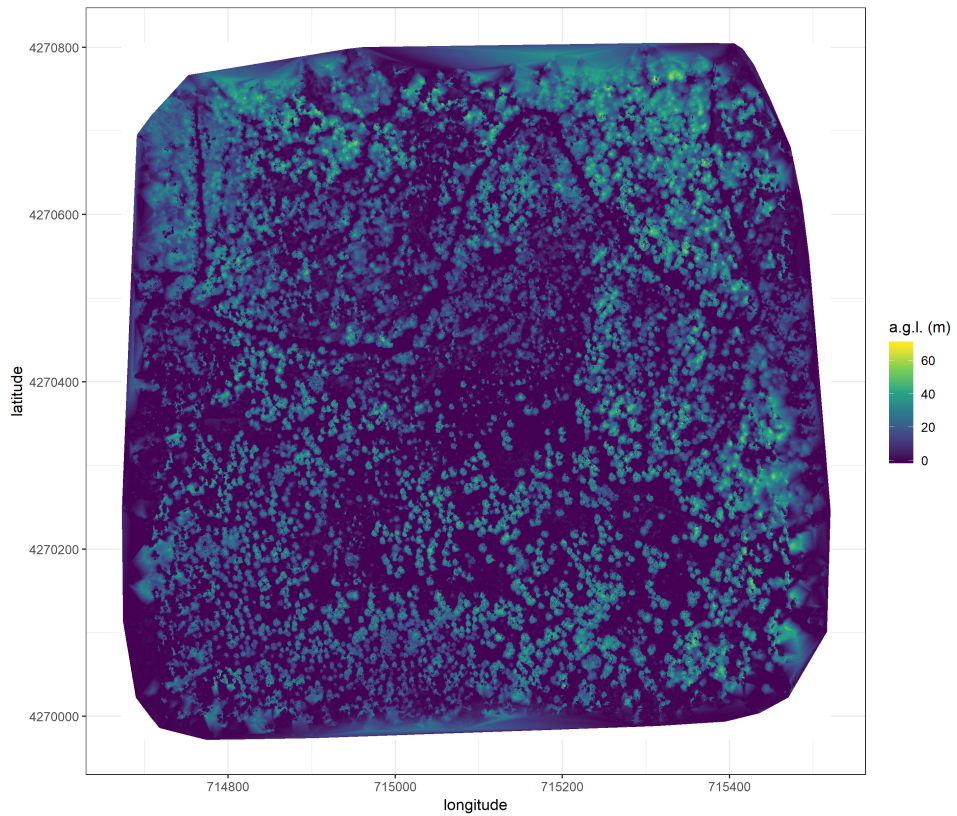


Figure 5: The canopy height model (CHM) is generated by subtracting the digital terrain model from the digital surface model. The CHM represents the height of all of the elevation above ground level.

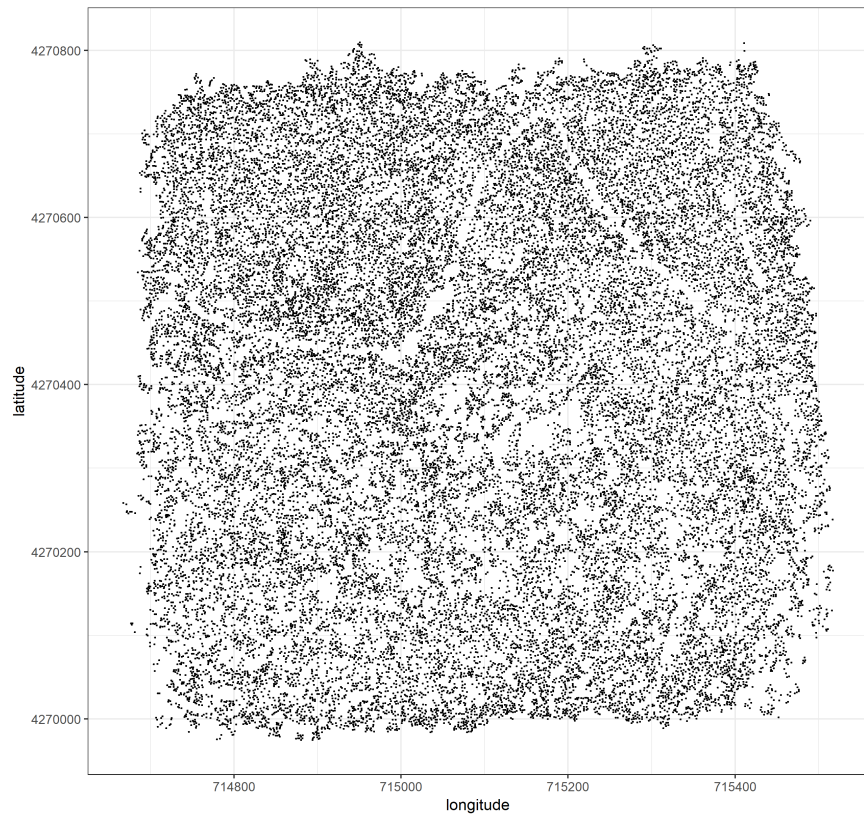


Figure 6: Tree locations are detected using the `lmfx` (Roussel et al. 2019) treetop detection algorithm on the dense point cloud.

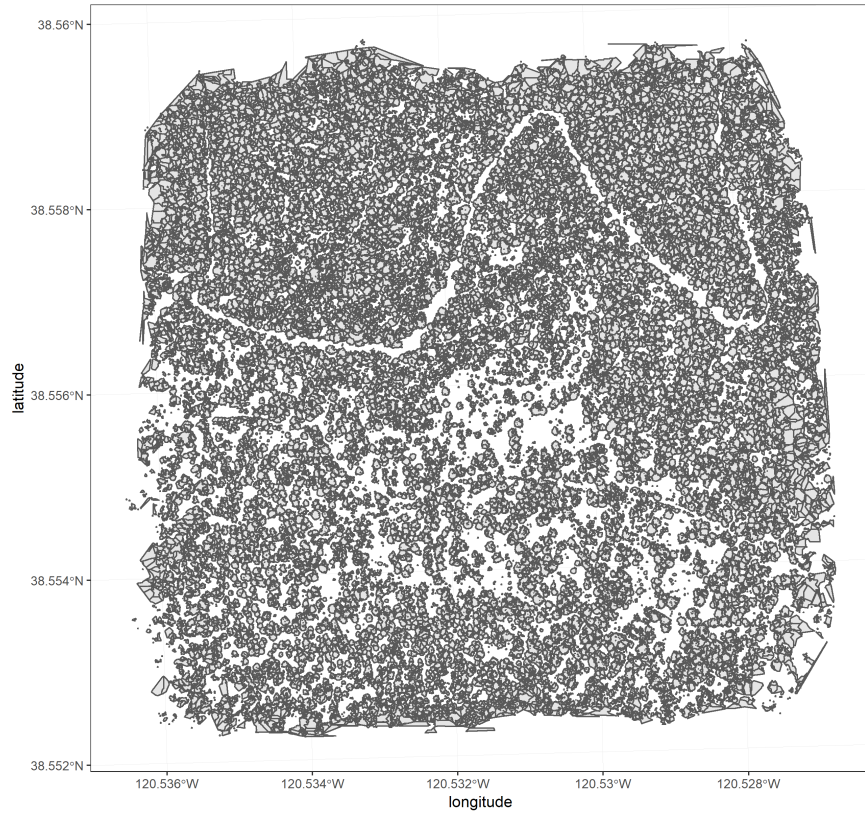


Figure 7: Individual crowns are delineated using a marker controlled watershed segmentation algorithm (Meyer and Beucher 1990, Plowright 2018) on the canopy height model (CHM) using the detected tree locations as a priority map. If the algorithm failed to delineate a crown for a tree that was identified in the tree detection step, a circular crown with a 0.5m buffer centered on point location of the detected tree was added as a crown. The crowns of snags were sometimes too small to be properly delineated, and the manually-created circular buffer

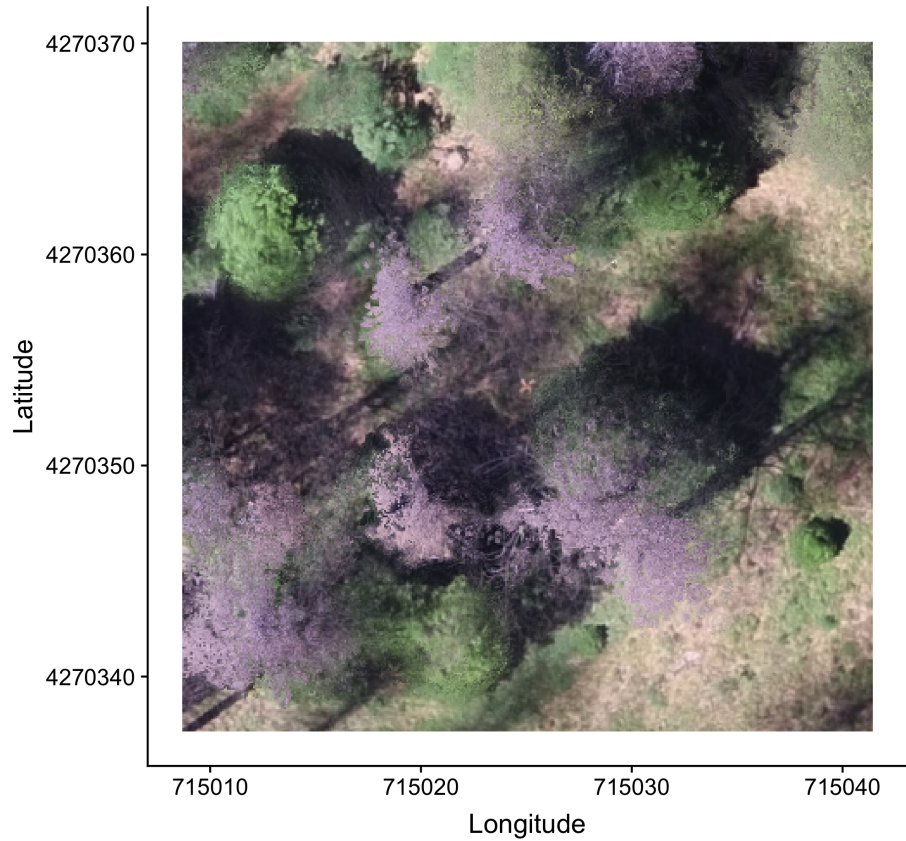


Figure 8: The orthomosaic for each site is generated with the Structure from Motion (SfM) processing, showing a top-down view of the whole survey area such that distances between objects in the scene are preserved and can be measured. This is a cropped example of an orthomosaic showing the orange X placed at exactly the plot center prior to flight.

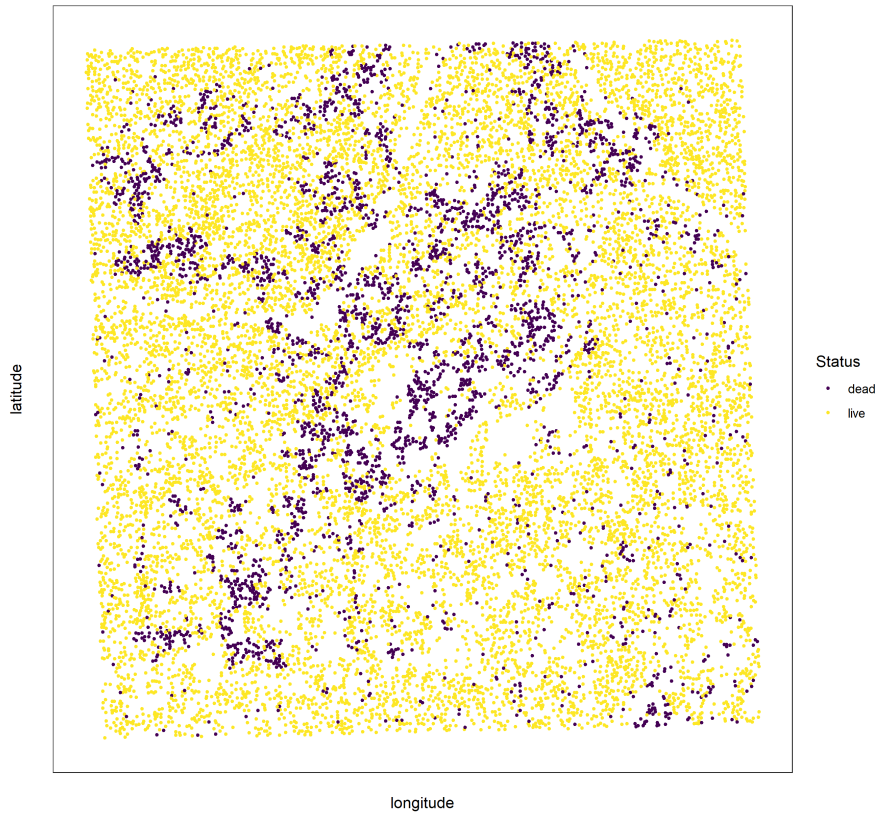


Figure 9: Each tree is classified as live or dead by extracting the pixel values from the 5 narrow bands of the Rededge3 camera (and 5 derived bands— see methods) in the orthomosaic within each segmented tree crown of the detected trees, taking their mean value, and using those means to predict live/dead status with a boosted logistic regression previously trained on a hand-classified set of segmented crowns from across the study area.

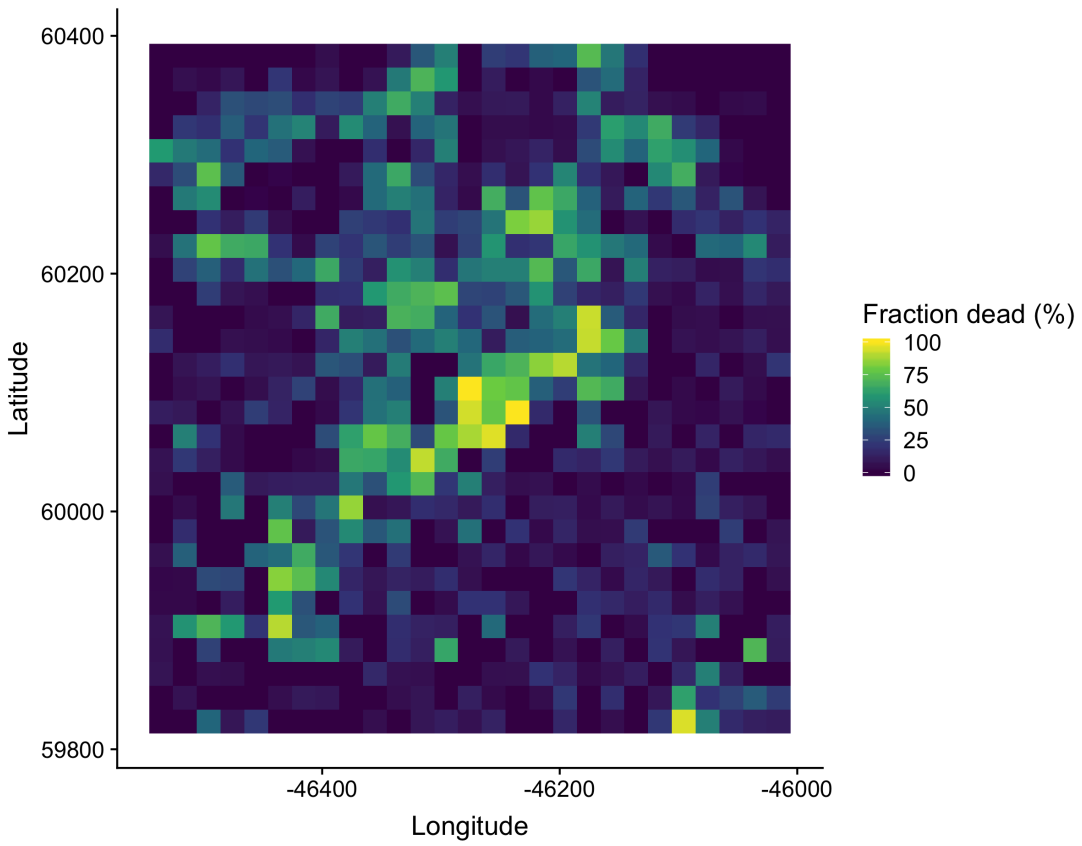


Figure 10: We rasterized the individual tree data by aggregating values to 20m x 20m cells. This example shows the proportion of dead trees per cell for the same example site as in the previous figures.

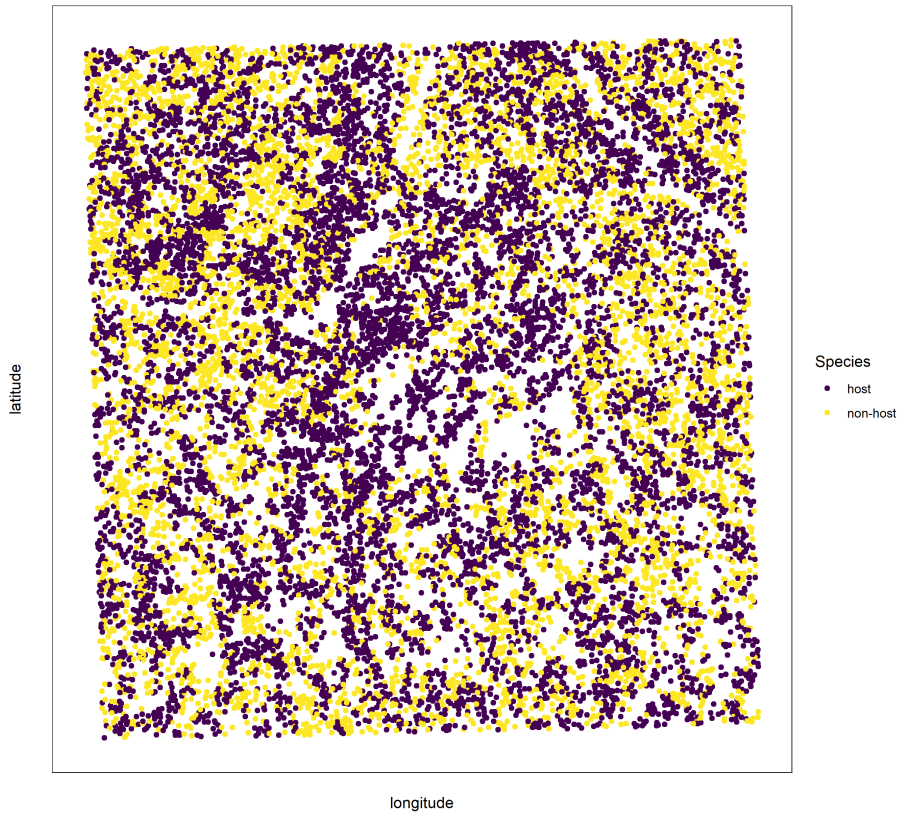


Figure 11: For each live tree, we classified its species using the same means of extracted pixel values across the 5 Rededge3 narrow bands (and 5 derived bands) as predictors in a regularized discriminant analysis previously trained on a hand-classified set of segmented crowns from across the study area. Host/non-host data were also rasterized as in the previous figure prior to analyses (not shown).

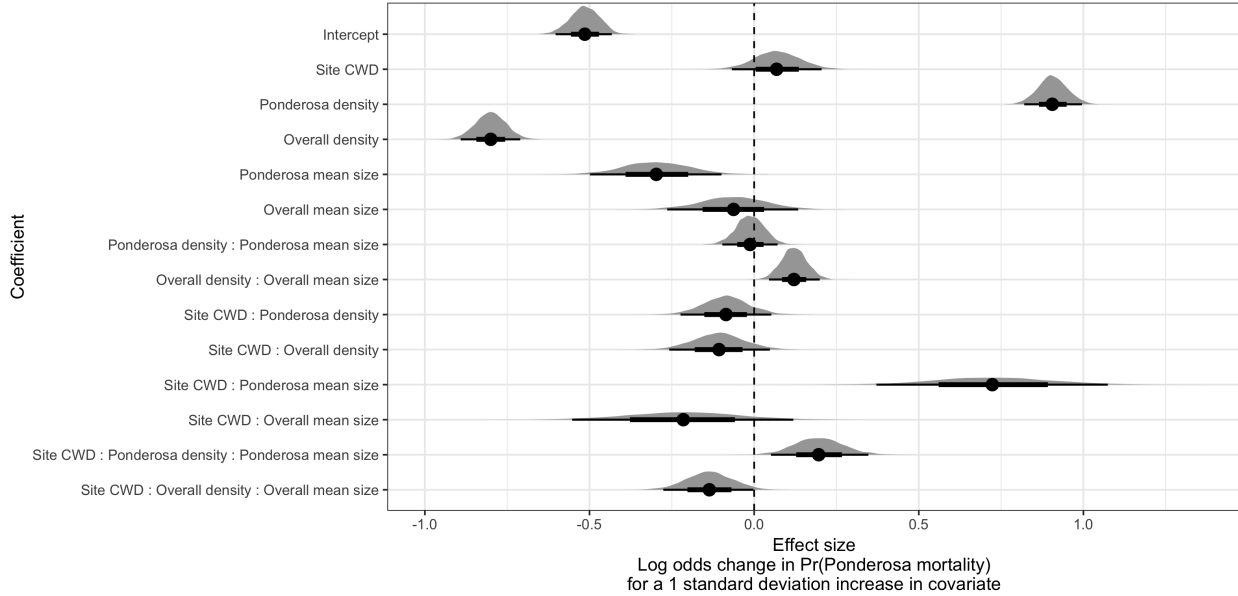


Figure 12: Posterior distributions of effect size from zero-inflated binomial model predicting the probability of ponderosa pine mortality in a 20m x 20m cell given forest structure characteristics of host trees and all trees within the cell, as well as a site-level climatic water deficit. The gray density distribution for each model covariate represents the density of the posterior distribution, the point underneath each density curve represents the median of the estimate, the bold interval surrounding the point estimate represents the 66% credible interval, and the thin interval surrounding the point estimate represents the 95% credible interval.

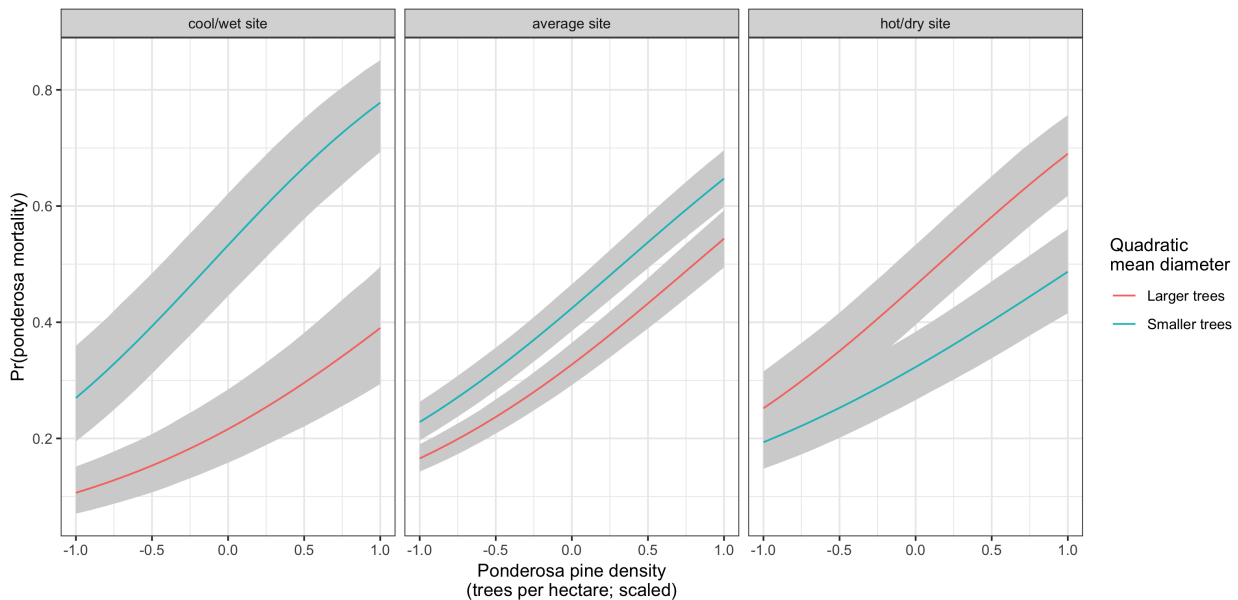


Figure 13: Line version of model results with 95% credible intervals showing primary influence of ponderosa pine structure on the probability of ponderosa pine mortality, and the interaction across climatic water deficit. The “larger trees” line represents the quadratic mean diameter of ponderosa pine 0.7 standard deviations above the mean, and the “smaller trees” line represents the quadratic mean diameter of ponderosa pine 0.7 standard deviations below the mean.

289 **Tree detection**

290 We found that the experimental `lmfx` algorithm with parameter values of `dist2d = 1` and `ws = 2.5` (Roussel  
291 et al. 2019) performed the best across 7 measures of forest structure as measured by Pearson's correlation  
292 with ground data (Table 2).

Table 3: Correlation and differences between the best performing tree detection algorithm (`lmfx` with `dist2d = 1` and `ws = 2.5`) and the ground data. An asterisk next to the correlation or RMSE indicates that this value was within 5% of the value of the best-performing algorithm/parameter set.

Forest structure metric	Correlation with ground	RMSE	Mean error	Median error
height (m); 25th percentile	0.16	8.46	-2.30	-1.16
height (m); mean	0.29	7.81*	-3.43	-2.29
height (m); 75th percentile	0.35	10.33*	-4.85	-3.98
dist to 1st nearest neighbor (m)	0.55*	1.16*	0.13	0.26
dist to 2nd nearest neighbor (m)	0.61*	1.70*	0.08	0.12
dist to 3rd nearest neighbor (m)	0.50	2.29	0.17	0.19
total tree count	0.67*	8.68*	0.37	2.00
count of trees > 15m	0.43	7.38	1.18	0.00
count of trees < 15m	0.58	8.42	-0.66	2.00

293 **Effect of local structure and regional climate on western pine beetle severity**

294 We detected no main effect of climatic water deficit on the probability of ponderosa pine mortality within  
295 each 20m x 20m cell.

296 We found a strong main effect of ponderosa pine local density, accounting for quadratic mean diameter of  
297 ponderosa pine, with greater density increasing the probability of ponderosa pine mortality. Conversely,  
298 we found a generally negative effect of quadratic mean diameter of ponderosa pine on the probability of  
299 ponderosa mortality, suggesting that the western pine beetle attacked smaller trees, on average. There was a  
300 strong positive interaction between the climatic water deficit and ponderosa pine quadratic mean diameter,  
301 such that larger trees were more likely to increase the probability of ponderosa mortality in hotter, drier sites.

302 We found negative main effects of overall tree density and overall quadratic mean diameter. There was a  
303 positive interaction between these variables, such that denser stands with larger trees did lead to greater  
304 ponderosa pine mortality.

305 **Spatial effects**

306 We were able to calculate the length scale of the spatial autocorrelation in the probability of ponderosa  
307 pine mortality at each site, accounting for forest structure and environmental factors. By fitting a separate  
308 approximate Gaussian process for each site on the interacting variables of the x- and y- position, we measured  
309 the spatial covariance inherent in the data, accounting for other factors. ## Discussion

310 **Closer spacing between potential host trees facilitates dispersal**

311 If this drives mortality patterns, then we'd expect the local density of ponderosa pine trees, accounting for  
312 other variables, to have a strong positive effect.

313 **Host preference for large trees**

314 If this drives mortality patterns, then we'd expect the quadratic mean diameter of ponderosa pine trees,  
315 accounting for other variables, to have a strong positive effect.

316 **Denser forests augment pheromone communication**

317 If this drives mortality patterns, then we'd expect the local density of all trees, accounting for other variables,  
318 to have a strong positive effect.

319 **Tree crowding leads to greater average water stress per tree**

320 If this drives mortality patterns, then we'd expect the quadratic mean dimater of all trees, accounting for  
321 other factors, to have a strong positive effect.

322 **Interaction between host density and host size**

323 A positive coefficient would indicate a combined effect of WPB preference for large trees and nearby host  
324 availability.

325 **Interaction between all tree density and all tree size**

326 A positive coefficient would indicate a combined effect of tree crowding and pheromone communication  
327 enhancement.

328 **Implications of forest structure/regional climate interactions**

329 We found that the probability of ponderosa pine mortality generally increased with local host availability  
330 (host density), but also interacted with both host size and regional climate such that the role of tree size  
331 became increasingly important in more climatically extreme sites. A smaller average tree size led to a lower  
332 probability of ponderosa mortality in cool/wet sites and a larger average tree size led to a greater probability  
333 of ponderosa mortality in hot/dry sites. These mortality patterns highlight a possible distinction in behavior  
334 between the recent western bark beetle activity across the gradient of climatic water deficit. Even in the most  
335 highly impacted forest stands (because our study sites were selected conditional on there being high levels of  
336 western pine beetle activity), there is still a detectable effect of tree size such that the smaller (presumably  
337 weaker) trees are getting killed in cooler/wetter sites, and the larger (presumably more well-defended) trees  
338 are getting killed more in the hotter/drier sites. So while mortality is high everywhere, there does appear to  
339 be a difference in the beetle choosiness across the climatic water deficit gradient.

340 **Similarities and differences with Fettig et al. (2019)**

341 Fettig et al. (2019) found positive relationship between number of trees killed and: total number of trees,  
342 total basal area, stand density index.

343 Fettig et al. (2019) found negative relationship between the proportion of trees killed and: total number of  
344 trees, stand density index.

345 Hayes et al. (2009) and Fettig et al. (2019) found measures of host availability explained less variation in  
346 mortality than measures of stand density.

347 Negrón et al. (2009) reported positive association of probability of ponderosa pine mortality and tree density  
348 during a drought in Arizona.

349 Effect of competition may be masked because drought was so extreme Fettig et al. (2019); Floyd et al.  
350 (2009), which is perhaps why we saw a counter-intuitive signal of increasing total basal area leading to lower  
351 probability of ponderosa pine mortality.

352 **Broader context around field plots**

353 We surveyed 9 square kilometers of forest representing ~450,000 trees along a broad environmental gradient  
354 of climatic water deficit. Site selection and small plot size can influence inference. For instance, Fettig et  
355 al. (2019) reported statistically undetectable differences in overall mortality in their plot network across 4  
356 national forests. By expanding the hectarage surveyed by a factor of 200, we detected dramatic differences in

357 overall mortality.

358 This is about more than sample size (though that helps). This is also about capturing the local disturbance  
359 phenomenon.

360 **Implications for future forest structure**

361 We have demonstrated that forest structure (local host density and size) affected the cumulative severity  
362 of the western pine beetle in the Sierra Nevada in the 2012 to 2015 drought and its aftermath. Clearly,  
363 this forest insect disturbance has reciprically impacted the forest structure, with uncertain consequences for  
364 long-term forest dynamics.

365 Small trees are getting killed in cooler/wetter sites, larger trees getting killed in hotter/drier sites. Perhaps  
366 the cooler/wetter sites are resisting even this massive disturbance event?

367 **Spatial effect**

368 The western pine beetle is known to exhibit strong aggregation and anti-aggregation behavior arising from  
369 its pheromone communication, and thus it is likely that the measured spatial covariance in this study is  
370 attributable in part to the magnitude of this effect at each site.

371 Some studies have suggested that “outbreak” conditions are distinguishable by clustered tree mortality, but  
372 this is perhaps challenging to tease apart (Raffa et al. 2008). Our modeling framework allows for a joint  
373 estimation of the effects of forest structure, environmental condition, and the spatial effect. This framework  
374 would be enhanced with confidence in individual tree level data, and a lot of it, along with a strong gradient  
375 of environmental conditions and forest structure.

376 We won’t interpret this measure of contagion, because the uncertainties in this particular study are too great  
377 (tree detection, species classification, dead trees all assumed to be WPB hosts, didn’t account for topographic  
378 effects which could also manifest as part of this spatial covariance process). We do suggest that this could be  
379 a meaningful and quantifiable means of assessing bark beetle “stage of outbreak”.

380 **Future spatial directions (will cut this; here for now so I can write it down elsewhere)**

381 Perhaps could also compare relative effect of individual tree spacing (Voronoi polygon area) with the length  
382 scale parameter at a certain site to get at a similar question. A big voronoi polygon area effect and a short  
383 covariance kernel tells us that it’s a water stress effect– a crowded tree gets attacked regardless of whether  
384 nearby trees were attacked. A small voronoi polygon area effect and a long covariance kernel tells us that the

385 mortality is patterned more based on there being spillover from nearby attacked neighbors instead of how  
386 crowded any given tree is. I expect we might see different relative magnitudes of voronoi polygon area and  
387 covariance kernel effects depending on CWD.

388 **Important considerations**

389 Cumulative effect of elevated insect activity, as mortality was spread out over 5 years and we surveyed at the  
390 end. All the detected dead trees were considered ponderosa pine— we know this is wrong. Only about 3 out  
391 of 4 dead trees in Fettig et al. (2019) were ponderosa.

392 **Room for improvement**

- 393 • Better geometry by using higher overlap, more spatially resolved images.
- 394 • Better image classification and scalability by using instrumentation having spectral overlap with more  
395 widely deployed instrumentation (e.g., Landsat).
- 396 • Better tree detection using machine learning approaches
- 397 • Our live/dead classifier works pretty well.
- 398 • Our species classifier could improve. Perhaps also using machine learning approaches.

399 (Seidl et al. 2015) (Preisler et al. 2017)

400 **References**

- 401 Baldwin, B. G., A. H. Thornhill, W. A. Freyman, D. D. Ackerly, M. M. Kling, N. Morueta-Holme, and B. D.  
402 Mishler. 2017. Species richness and endemism in the native flora of California. American Journal of Botany  
403 104:487–501.
- 404 Brooks, S. P., and A. Gelman. 1998. General Methods for Monitoring Convergence of Iterative Simulations.  
405 Journal of Computational and Graphical Statistics 7:434.
- 406 Bürkner, P.-C. 2017. **Brms** : An *R* Package for Bayesian Multilevel Models Using *Stan*. Journal of Statistical  
407 Software 80.
- 408 Clevers, J., and A. Gitelson. 2013. Remote estimation of crop and grass chlorophyll and nitrogen content using  
409 red-edge bands on Sentinel-2 and -3. International Journal of Applied Earth Observation and Geoinformation  
410 23:344–351.
- 411 Coops, N. C., M. Johnson, M. A. Wulder, and J. C. White. 2006. Assessment of QuickBird high spatial  
412 resolution imagery to detect red attack damage due to mountain pine beetle infestation. Remote Sensing of

- 413 Environment 103:67–80.
- 414 DJI. 2015a. Zenmuse X3 - Creativity Unleashed. <https://www.dji.com/zenmuse-x3/info>.
- 415 DJI. 2015b. DJI - The World Leader in Camera Drones/Quadcopters for Aerial Photography. <https://www.dji.com/matrice100/info>.
- 416
- 417 Easy, D. M. 2018. Map Pilot for DJI. <https://itunes.apple.com/us/app/map-pilot-for-dji/id1014765000?mt=8>.
- 418 Eysn, L., M. Hollaus, E. Lindberg, F. Berger, J.-M. Monnet, M. Dalponte, M. Kobal, M. Pellegrini, E.
- 419 Lingua, D. Mongus, and N. Pfeifer. 2015. A Benchmark of Lidar-Based Single Tree Detection Methods Using
- 420 Heterogeneous Forest Data from the Alpine Space. Forests 6:1721–1747.
- 421 Farr, T. G., P. A. Rosen, E. Caro, R. Crippen, R. Duren, S. Hensley, M. Kobrick, M. Paller, E. Rodriguez, L.
- 422 Roth, D. Seal, S. Shaffer, J. Shimada, J. Umland, M. Werner, M. Oskin, D. Burbank, and D. Alsdorf. 2007.
- 423 The Shuttle Radar Topography Mission. Reviews of Geophysics 45.
- 424 Fettig, C. J. 2012. Chapter 2: Forest health and bark beetles. *in* Managing Sierra Nevada Forests. PSW-
- 425 GTR-237. USDA Forest Service.
- 426 Fettig, C. J., L. A. Mortenson, B. M. Bulaon, and P. B. Foulk. 2019. Tree mortality following drought in the
- 427 central and southern Sierra Nevada, California, U.S. Forest Ecology and Management 432:164–178.
- 428 Flint, L. E., A. L. Flint, J. H. Thorne, and R. Boynton. 2013. Fine-scale hydrologic modeling for regional land-
- 429 scape applications: The California Basin Characterization Model development and performance. Ecological
- 430 Processes 2:25.
- 431 Floyd, M. L., M. Clifford, N. S. Cobb, D. Hanna, R. Delph, P. Ford, and D. Turner. 2009. Relationship of
- 432 stand characteristics to drought-induced mortality in three Southwestern piñonJuniper woodlands. Ecological
- 433 Applications 19:1223–1230.
- 434 Gabry, J., D. Simpson, A. Vehtari, M. Betancourt, and A. Gelman. 2019. Visualization in Bayesian workflow.
- 435 Journal of the Royal Statistical Society: Series A (Statistics in Society) 182:389–402.
- 436 Gitelson, A., and M. N. Merzlyak. 1994. Spectral Reflectance Changes Associated with Autumn Senescence
- 437 of Aesculus hippocastanum L. and Acer platanoides L. Leaves. Spectral Features and Relation to Chlorophyll
- 438 Estimation. Journal of Plant Physiology 143:286–292.
- 439 Hayes, C. J., C. J. Fettig, and L. D. Merrill. 2009. Evaluation of Multiple Funnel Traps and Stand
- 440 Characteristics for Estimating Western Pine Beetle-Caused Tree Mortality. Journal of Economic Entomology

- <sup>441</sup> 102:2170–2182.
- <sup>442</sup> Hijmans, R. J., J. van Etten, M. Sumner, J. Cheng, A. Bevan, R. Bivand, L. Busetto, M. Canty, D. Forrest,  
<sup>443</sup> A. Ghosh, D. Goliche, J. Gray, J. A. Greenberg, P. Hiemstra, I. for M. A. Geosciences, C. Karney, M.  
<sup>444</sup> Mattiuzzi, S. Mosher, J. Nowosad, E. Pebesma, O. P. Lamigueiro, E. B. Racine, B. Rowlingson, A. Shortridge,  
<sup>445</sup> B. Venables, and R. Wueest. 2019. *Raster: Geographic Data Analysis and Modeling*.
- <sup>446</sup> Hunziker, P. 2017. *Velox: Fast Raster Manipulation and Extraction*.
- <sup>447</sup> Jakubowski, M. K., W. Li, Q. Guo, and M. Kelly. 2013. Delineating Individual Trees from Lidar Data: A  
<sup>448</sup> Comparison of Vector- and Raster-based Segmentation Approaches. *Remote Sensing* 5:4163–4186.
- <sup>449</sup> Kane, V. R., M. P. North, J. A. Lutz, D. J. Churchill, S. L. Roberts, D. F. Smith, R. J. McGaughey, J. T.  
<sup>450</sup> Kane, and M. L. Brooks. 2014. Assessing fire effects on forest spatial structure using a fusion of Landsat and  
<sup>451</sup> airborne LiDAR data in Yosemite National Park. *Remote Sensing of Environment* 151:89–101.
- <sup>452</sup> Kuhn, M. 2008. Building Predictive Models in R Using the caret Package. *Journal of Statistical Software*  
<sup>453</sup> 28:1–26.
- <sup>454</sup> Larson, A. J., and D. Churchill. 2012. Tree spatial patterns in fire-frequent forests of western North America,  
<sup>455</sup> including mechanisms of pattern formation and implications for designing fuel reduction and restoration  
<sup>456</sup> treatments. *Forest Ecology and Management* 267:74–92.
- <sup>457</sup> Li, W., Q. Guo, M. K. Jakubowski, and M. Kelly. 2012. A New Method for Segmenting Individual Trees  
<sup>458</sup> from the Lidar Point Cloud. *Photogrammetric Engineering & Remote Sensing* 78:75–84.
- <sup>459</sup> Meyer, F., and S. Beucher. 1990. Morphological segmentation. *Journal of Visual Communication and Image  
460 Representation* 1:21–46.
- <sup>461</sup> Micasense. 2015. MicaSense. <https://support.micasense.com/hc/en-us/articles/215261448-RedEdge-User-Manual-PDF-Download>
- <sup>462</sup> Millar, C. I., and N. L. Stephenson. 2015. Temperate forest health in an era of emerging megadisturbance.  
<sup>463</sup> *Science* 349:823–826.
- <sup>464</sup> Morris, J. L., S. Cottrell, C. J. Fettig, W. D. Hansen, R. L. Sherriff, V. A. Carter, J. L. Clear, J. Clement, R.  
<sup>465</sup> J. DeRose, J. A. Hicke, P. E. Higuera, K. M. Mattor, A. W. R. Seddon, H. T. Seppä, J. D. Stednick, and S.  
<sup>466</sup> J. Seybold. 2017. Managing bark beetle impacts on ecosystems and society: Priority questions to motivate  
<sup>467</sup> future research. *Journal of Applied Ecology* 54:750–760.
- <sup>468</sup> Negrón, J. F., J. D. McMillin, J. A. Anhold, and D. Coulson. 2009. Bark beetle-caused mortality in a

- 469 drought-affected ponderosa pine landscape in Arizona, USA. Forest Ecology and Management 257:1353–1362.
- 470 North, M. P., S. L. Stephens, B. M. Collins, J. K. Agee, G. Aplet, J. F. Franklin, and P. Z. Fule. 2015.
- 471 Reform forest fire management. Science 349:1280–1281.
- 472 Pau, G., F. Fuchs, O. Sklyar, M. Boutros, and W. Huber. 2010. EBImagean R package for image processing
- 473 with applications to cellular phenotypes. Bioinformatics 26:979–981.
- 474 Pebesma, E., R. Bivand, E. Racine, M. Sumner, I. Cook, T. Keitt, R. Lovelace, H. Wickham, J. Ooms, K.
- 475 Müller, and T. L. Pedersen. 2019. Sf: Simple Features for R.
- 476 Plowright, A. 2018. ForestTools: Analyzing Remotely Sensed Forest Data.
- 477 Popescu, S. C., and R. H. Wynne. 2004. Seeing the Trees in the Forest: Using Lidar and Multispectral Data
- 478 Fusion with Local Filtering and Variable Window Size for Estimating Tree Height. PHOTOGGRAMMETRIC
- 479 ENGINEERING:16.
- 480 Preisler, H. K., N. E. Grulke, Z. Heath, and S. L. Smith. 2017. Analysis and out-year forecast of beetle,
- 481 borer, and drought-induced tree mortality in California. Forest Ecology and Management. 399: 166–178
- 482 399:166–178.
- 483 R Core Team. 2018. R: A Language and Environment for Statistical Computing. R Foundation for Statistical
- 484 Computing, Vienna, Austria.
- 485 Raffa, K. F., B. H. Aukema, B. J. Bentz, A. L. Carroll, J. A. Hicke, M. G. Turner, and W. H. Romme. 2008.
- 486 Cross-scale Drivers of Natural Disturbances Prone to Anthropogenic Amplification: The Dynamics of Bark
- 487 Beetle Eruptions. BioScience 58:501–517.
- 488 Raffa, K. F., J.-C. Grégoire, and B. Staffan Lindgren. 2015. Natural History and Ecology of Bark Beetles.
- 489 Pages 1–40 in Bark Beetles. Elsevier.
- 490 Rouse, W., R. H. Haas, W. Deering, and J. A. Schell. 1973. MONITORING THE VERNAL ADVANCEMENT
- 491 AND RETROGRADATION (GREEN WAVE EFFECT) OF NATURAL VEGETATION. Type II Report,
- 492 Goddard Space Flight Center, Greenbelt, MD, USA.
- 493 Roussel, J.-R. 2019. lidRplugins: Extra functions and algorithms for lidR package.
- 494 Roussel, J.-R., D. A. (the documentation), F. D. B. (bugs and improved catalog features), and A. S. M. (.
- 495 lassnags). 2019. lidR: Airborne LiDAR Data Manipulation and Visualization for Forestry Applications.
- 496 Seidl, R., J. Müller, T. Hothorn, C. Bässler, M. Heurich, and M. Kautz. 2015. Small beetle, large-scale
- 497 drivers: How regional and landscape factors affect outbreaks of the European spruce bark beetle. The Journal

- 498 of applied ecology 53:530–540.
- 499 Shiklomanov, A. N., B. A. Bradley, K. M. Dahlin, A. M. Fox, C. M. Gough, F. M. Hoffman, E. M. Middleton,  
500 S. P. Serbin, L. Smallman, and W. K. Smith. 2019. Enhancing global change experiments through integration  
501 of remote-sensing techniques. *Frontiers in Ecology and the Environment* 0.
- 502 Shin, P., T. Sankey, M. Moore, and A. Thode. 2018. Evaluating Unmanned Aerial Vehicle Images for  
503 Estimating Forest Canopy Fuels in a Ponderosa Pine Stand. *Remote Sensing* 10:1266.
- 504 Stephenson, N. 1998. Actual evapotranspiration and deficit: Biologically meaningful correlates of vegetation  
505 distribution across spatial scales. *Journal of Biogeography* 25:855–870.
- 506 Stephenson, N. L., A. J. Das, N. J. Ampersee, and B. M. Bulaon. 2019. Which trees die during drought?  
507 The key role of insect host-tree selection. *Journal of Ecology*:75.
- 508 USDAFS. 2019, February 11. Press Release: Survey finds 18 million trees died in California in 2018.  
509 [https://www.fs.usda.gov/Internet/FSE\\_DOCUMENTS/FSEPRD609321.pdf](https://www.fs.usda.gov/Internet/FSE_DOCUMENTS/FSEPRD609321.pdf).
- 510 Vega, C., A. Hamrouni, S. El Mokhtari, J. Morel, J. Bock, J. P. Renaud, M. Bouvier, and S. Durrieu. 2014.  
511 PTrees: A point-based approach to forest tree extraction from lidar data. *International Journal of Applied  
512 Earth Observation and Geoinformation* 33:98–108.
- 513 Young, D. J. N., J. T. Stevens, J. M. Earles, J. Moore, A. Ellis, A. L. Jirka, and A. M. Latimer. 2017.  
514 Long-term climate and competition explain forest mortality patterns under extreme drought. *Ecology Letters*  
515 20:78–86.
- 516 Zhang, W., J. Qi, P. Wan, H. Wang, D. Xie, X. Wang, and G. Yan. 2016. An Easy-to-Use Airborne LiDAR  
517 Data Filtering Method Based on Cloth Simulation. *Remote Sensing* 8:501.